# Ore Deposits

## Origin, Exploration, and Exploitation

Sophie Decrée and Laurence Robb
*Editors*

AGU100 ADVANCING EARTH AND SPACE SCIENCE

WILEY

Geophysical Monograph Series

**190** **The Stratosphere: Dynamics, Transport, and Chemistry** *L. M. Polvani, A. H. Sobel, and D. W. Waugh (Eds.)*
**191** **Rainfall: State of the Science** *Firat Y. Testik and Mekonnen Gebremichael (Eds.)*
**192** **Antarctic Subglacial Aquatic Environments** *Martin J. Siegert, Mahlon C. Kennicut II, and Robert A. Bindschadler (Eds.)*
**193** **Abrupt Climate Change: Mechanisms, Patterns, and Impacts** *Harunur Rashid, Leonid Polyak, and Ellen Mosley-Thompson (Eds.)*
**194** **Stream Restoration in Dynamic Fluvial Systems: Scientific Approaches, Analyses, and Tools** *Andrew Simon, Sean J. Bennett, and Janine M. Castro (Eds.)*
**195** **Monitoring and Modeling the Deepwater Horizon Oil Spill: A Record-Breaking Enterprise** *Yonggang Liu, Amy MacFadyen, Zhen-Gang Ji, and Robert H. Weisberg (Eds.)*
**196** **Extreme Events and Natural Hazards: The Complexity Perspective** *A. Surjalal Sharma, Armin Bunde, Vijay P. Dimri, and Daniel N. Baker (Eds.)*
**197** **Auroral Phenomenology and Magnetospheric Processes: Earth and Other Planets** *Andreas Keiling, Eric Donovan, Fran Bagenal, and Tomas Karlsson (Eds.)*
**198** **Climates, Landscapes, and Civilizations** *Liviu Giosan, Dorian Q. Fuller, Kathleen Nicoll, Rowan K. Flad, and Peter D. Clift (Eds.)*
**199** **Dynamics of the Earth's Radiation Belts and Inner Magnetosphere** *Danny Summers, Ian R. Mann, Daniel N. Baker, and Michael Schulz (Eds.)*
**200** **Lagrangian Modeling of the Atmosphere** *John Lin (Ed.)*
**201** **Modeling the Ionosphere-Thermosphere** *Jospeh D. Huba, Robert W. Schunk, and George V. Khazanov (Eds.)*
**202** **The Mediterranean Sea: Temporal Variability and Spatial Patterns** *Gian Luca Eusebi Borzelli, Miroslav Gacic, Piero Lionello, and Paola Malanotte-Rizzoli (Eds.)*
**203** **Future Earth – Advancing Civic Understanding of the Anthropocene** *Diana Dalbotten, Gillian Roehrig, and Patrick Hamilton (Eds.)*
**204** **The Galápagos: A Natural Laboratory for the Earth Sciences** *Karen S. Harpp, Eric Mittelstaedt, Noémi d'Ozouville, and David W. Graham (Eds.)*
**205** **Modeling Atmospheric and Oceanic Flows: Insightsfrom Laboratory Experiments and Numerical Simulations** *Thomas von Larcher and Paul D. Williams (Eds.)*
**206** **Remote Sensing of the Terrestrial Water Cycle** *Venkat Lakshmi (Ed.)*
**207** **Magnetotails in the Solar System** *Andreas Keiling, Caitríona Jackman, and Peter Delamere (Eds.)*
**208** **Hawaiian Volcanoes: From Source to Surface** Rebecca *Carey, Valerie Cayol, Michael Poland, and Dominique Weis (Eds.)*
**209** **Sea Ice: Physics, Mechanics, and Remote Sensing** *Mohammed Shokr and Nirmal Sinha (Eds.)*
**210** **Fluid Dynamics in Complex Fractured-Porous Systems** *Boris Faybishenko, Sally M. Benson, and John E. Gale (Eds.)*
**211** **Subduction Dynamics: From Mantle Flow to Mega Disasters** *Gabriele Morra, David A. Yuen, Scott King, Sang Mook Lee, and Seth Stein (Eds.)*
**212** **The Early Earth: Accretion and Differentiation** *James Badro and Michael Walter (Eds.)*
**213** **Global Vegetation Dynamics: Concepts and Applications in the MC1 Model** *Dominique Bachelet and David Turner (Eds.)*
**214** **Extreme Events: Observations, Modeling and Economics** *Mario Chavez, Michael Ghil, and Jaime Urrutia-Fucugauchi (Eds.)*
**215** **Auroral Dynamics and Space Weather** *Yongliang Zhang and Larry Paxton (Eds.)*
**216** **Low-Frequency Waves in Space Plasmas** *Andreas Keiling, Dong-Hun Lee, and Valery Nakariakov (Eds.)*
**217** **Deep Earth: Physics and Chemistry of the Lower Mantle and Core** *Hidenori Terasaki and Rebecca A. Fischer (Eds.)*
**218** **Integrated Imaging of the Earth: Theory and Applications** *Max Moorkamp, Peter G. Lelievre, Niklas Linde, and Amir Khan (Eds.)*
**219** **Plate Boundaries and Natural Hazards** *Joao Duarte and Wouter Schellart (Eds.)*
**220** **Ionospheric Space Weather: Longitude and Hemispheric Dependences and Lower Atmosphere Forcing Timothy Fuller-Rowell**, *Endawoke Yizengaw, Patricia H. Doherty, and Sunanda Basu (Eds.)*
**221** **Terrestrial Water Cycle and Climate Change Natural and Human-Induced Impacts** *Qiuhong Tang and Taikan Oki (Eds.)*
**222** **Magnetosphere-Ionosphere Coupling in the Solar System** *Charles R. Chappell, Robert W. Schunk, Peter M. Banks, James L. Burch, and Richard M. Thorne (Eds.)*
**223** **Natural Hazard Uncertainty Assessment: Modeling and Decision Support** *Karin Riley, Peter Webley, and Matthew Thompson (Eds.)*
**224** **Hydrodynamics of Time-Periodic Groundwater Flow: Diffusion Waves in Porous Media** *Joe S. Depner and Todd C. Rasmussen (Auth.)*
**225** **Active Global Seismology** *Ibrahim Cemen and Yucel Yilmaz (Eds.)*
**226** **Climate Extremes** *Simon Wang (Ed.)*
**227** **Fault Zone Dynamic Processes** *Marion Thomas (Ed.)*
**228** **Flood Damage Survey and Assessment: New Insights from Research and Practice** *Daniela Molinari, Scira Menoni, and Francesco Ballio (Eds.)*
**229** **Water-Energy-Food Nexus – Principles and Practices** *P. Abdul Salam, Sangam Shrestha, Vishnu Prasad Pandey, and Anil K Anal (Eds.)*
**230** **Dawn–Dusk Asymmetries in Planetary Plasma Environments** *Stein Haaland, Andrei Rounov, and Colin Forsyth (Eds.)*
**231** **Bioenergy and Land Use Change** *Zhangcai Qin, Umakant Mishra, and Astley Hastings (Eds.)*
**232** **Microstructural Geochronology: Planetary Records Down to Atom Scale** *Desmond Moser, Fernando Corfu, James Darling, Steven Reddy, and Kimberly Tait (Eds.)*
**233** **Global Flood Hazard: Applications in Modeling, Mapping and Forecasting** *Guy Schumann, Paul D. Bates, Giuseppe T. Aronica, and Heiko Apel (Eds.)*
**234** **Pre-Earthquake Processes: A Multidisciplinary Approach to Earthquake Prediction Studies** *Dimitar Ouzounov, Sergey Pulinets, Katsumi Hattori, and Patrick Taylor (Eds.)*
**235** **Electric Currents in Geospace and Beyond** *Andreas Keiling, Octav Marghitu, and Michael Wheatland (Eds.)*
**236** **Quantifying Uncertainty in Subsurface Systems** *Céline Scheidt, Lewis Li, and Jef Caers (Eds.)*
**237** **Petroleum Engineering** *Moshood Sanni (Ed.)*
**238** **Geological Carbon Storage: Subsurface Seals and Caprock Integrity** *Stéphanie Vialle, Jonathan Ajo-Franklin, and J. William Carey (Eds.)*
**239** **Lithospheric Discontinuities** *Huaiyu Yuan and Barbara Romanowicz (Eds.)*
**240** **Chemostratigraphy Across Major Chronological Eras** *Alcides N.Sial, Claudio Gaucher, Muthuvairavasamy Ramkumar, and Valderez Pinto Ferreira (Eds.)*
**241** **Mathematical Geoenergy:Discovery, Depletion, and Renewal** *Paul Pukite, Dennis Coyne, and Daniel Challou (Eds.)*

Geophysical Monograph 242

# Ore Deposits
## *Origin, Exploration, and Exploitation*

**Sophie Decrée**
**Laurence Robb**
***Editors***

This Work is a co-publication of the American Geophysical Union and John Wiley and Sons, Inc.

AGU 100
ADVANCING EARTH AND SPACE SCIENCE

WILEY

This Work is a co-publication between the American Geophysical Union and John Wiley & Sons, Inc.

This edition first published 2019 by John Wiley & Sons, Inc., 111 River Street, Hoboken, NJ 07030, USA and the American Geophysical Union, 2000 Florida Avenue, N.W., Washington, D.C. 20009

© 2019 American Geophysical Union

All rights reserved. No part of this publication may be reproduced, stored in a retrieval system, or transmitted, in any form or by any means, electronic, mechanical, photocopying, recording, or otherwise, except as permitted by law. Advice on how to obtain permission to reuse material from this title is available at http://www.wiley.com/go/permissions

**Published under the aegis of the AGU Publications Committee**

Brooks Hanson, Executive Vice President, Science
Lisa Tauxe, Chair, Publications Committee
For details about the American Geophysical Union visit us at www.agu.org.

**Wiley Global Headquarters**
111 River Street, Hoboken, NJ 07030, USA
For details of our global editorial offices, customer services, and more information about Wiley products visit us at www.wiley.com.

**Limit of Liability/Disclaimer of Warranty**
While the publisher and authors have used their best efforts in preparing this work, they make no representations or warranties with respect to the accuracy or completeness of the contents of this work and specifically disclaim all warranties, including without limitation any implied warranties of merchantability or fitness for a particular purpose. No warranty may be created or extended by sales representatives, written sales materials, or promotional statements for this work. The fact that an organization, website, or product is referred to in this work as a citation and/or potential source of further information does not mean that the publisher and authors endorse the information or services the organization, website, or product may provide or recommendations it may make. This work is sold with the understanding that the publisher is not engaged in rendering professional services. The advice and strategies contained herein may not be suitable for your situation. You should consult with a specialist where appropriate. Neither the publisher nor authors shall be liable for any loss of profit or any other commercial damages, including but not limited to special, incidental, consequential, or other damages. Further, readers should be aware that websites listed in this work may have changed or disappeared between when this work was written and when it is read.

**Library of Congress Cataloging-in-Publication data is available**

ISBN: 9781119290537

Cover image: Courtesy of Laurence Robb
Cover design: Wiley

Set in 10/12pt Times New Roman by SPi Global, Pondicherry, India

10 9 8 7 6 5 4 3 2 1

# CONTENTS

# CONTRIBUTORS

**Jean-Marc Baele**
Department of Geology and Applied Geology
University of Mons
Mons, Belgium

**Shaun L. L. Barker**
School of Science
University of Waikato,
Hamilton, New Zealand;
Mineral Deposit Research Unit
University of British Columbia
Vancouver, BC, Canada;
Centre for Ore Deposit and Earth Sciences
University of Tasmania
Hobart, Tasmania

**Tamara B. Bayanova**
Geological Institute
Kola Science Centre
Russian Academy of Sciences (GI KSC RAS)
Apatity, Russia

**Victor V. Chashchin**
Geological Institute
Kola Science Centre
Russian Academy of Sciences (GI KSC RAS)
Apatity, Russia

**Janine Cole**
School of Geosciences
University of the Witwatersrand
Johannesburg, South Africa;
Geophysics and Remote Sensing Unit
Council for Geoscience
Silverton, Pretoria, South Africa

**G. R. J. Cooper**
School of Geosciences
University of the Witwatersrand
Johannesburg, South Africa

**L. Corriveau**
Geological Survey of Canada
Natural Resources Canada
Québec, QC, Canada

**W. J. Davis**
Geological Survey of Canada
Natural Resources Canada
Ottawa, ON, Canada

**Sophie Decrée**
Geological Survey of Belgium
Royal Belgian Institute of Natural Sciences
Brussels, Belgium

**Stijn Dewaele**
Department of Geology and Mineralogy
Royal Museum for Central Africa
Tervuren, Belgium;
Department of Geology and Soil Science
Ghent University
Ghent, Belgium

**Gregory M. Dipple**
Mineral Deposit Research Unit
University of British Columbia
Vancouver, BC, Canada

**R. J. Durrheim**
University of the Witwatersrand
School of Geosciences
Johannesburg, South Africa

**Niels Hulsbosch**
KU Leuven
Geodynamics and Geofluids Research Group
Department of Earth and Environmental Sciences
Leuven, Belgium

**E. J. Hunt**
University of the Witwatersrand
School of Geosciences
Johannesburg, South Africa

**Alexey U. Korchagin**
Geological Institute, Kola Science Centre
Russian Academy of Sciences (GI KSC RAS),
Apatity, Russia;
JSC "Pana,"
Apatity, Russia

**John N. Ludden**
British Geological Survey
Keyworth, Nottingham, UK

**M. S. Manzi**
University of the Witwatersrand
School of Geosciences
Johannesburg, South Africa

**S. Master**
Economic Geology Research Institute
School of Geosciences
University of the Witwatersrand
Johannesburg, South Africa

**Ryan Mathur**
Department of Geology
Juniata College
Huntingdon, Pennsylvania, USA

**Maarten Minnen**
KU Leuven
Geodynamics and Geofluids Research Group
Department of Earth and Environmental Sciences
Leuven, Belgium

**Alexander F. Mitrofanov**
SRK Consulting
Toronto, Canada

**Felix P. Mitrofanov**
Geological Institute
Kola Science Centre
Russian Academy of Sciences (GI KSC RAS)
Apatity, Russia

**J.-F. Montreuil**
Formerly Institut National de la Recherche Scientifique
Québec, QC, Canada;
Red Pine Exploration Inc.
Toronto, ON, Canada

**Philippe Muchez**
KU Leuven
Geodynamics and Geofluids Research Group
Department of Earth and Environmental Sciences
Leuven, Belgium

**N. M. Ndhlovu**
School of Geosciences
University of the Witwatersrand
Johannesburg, South Africa

**Lyudmila I. Nerovich**
Geological Institute
Kola Science Centre
Russian Academy of Sciences (GI KSC RAS)
Apatity, Russia

**E. G. Potter**
Geological Survey of Canada
Natural Resources Canada
Ottawa, ON, Canada

**Brian Rusk**
Department of Geology
Western Washington University
Bellingham, Washington, USA

**Stephanie E. Scheiber-Enslin**
School of Geosciences
University of the Witwatersrand
Johannesburg, South Africa

**Pavel A. Serov**
Geological Institute
Kola Science Centre
Russian Academy of Sciences (GI KSC RAS)
Apatity, Russia

**Da Wang**
State Key Laboratory of Geological Processes
and Mineral Resources
School of Earth Sciences and Resources
China University of Geosciences
Beijing, China

**Susan J. Webb**
School of Geosciences
University of the Witwatersrand
Johannesburg, South Africa

**Dmitry V. Zhirov**
Geological Institute
Kola Science Centre
Russian Academy of Sciences (GI KSC RAS)
Apatity, Russia

# PREFACE

The volatility of financial markets over the past decade has had a major impact on the upstream sector of the global resource industry. Exploration and replenishment of natural resources have not kept pace with consumption, and the declining rate of discovery of new, viable mineral deposits is cause for concern. Coupled with this is the fact that world-class mineral deposits are increasingly difficult to find because large, shallow ores have largely been discovered. A major challenge of the 21st century, therefore, is how to locate buried mineral deposits that do not have a footprint at the surface, and also how to identify new sources of mineral wealth.

Recent trends in exploration and mining have seen a number of amazing innovations, exemplified by technologies that have, for example, enabled the mining of massive sulphide deposits on the ocean floor. Even more astounding are the developments aimed at exploiting asteroids from near-Earth orbits. While many might see these innovations as futuristic, they are nevertheless counterbalanced by the ability of geoscientists to continue pushing the frontiers of mineral exploration and seek new land-bound metallotects, as well as to develop innovative methods for detecting metal anomalies under cover. This book brings together a variety of papers that, in Section I, highlight the features of less conventional mineral deposit styles that offer alternative exploration opportunities, and, in Section II, describe some of the recent technological advances that will assist in the future discovery of mineral deposits.

Whereas most of the world's mineral exploration is still focused on well-trodden metallotects, such as magmatic arcs and stable cratonic blocks, Section I emphasizes the features of atypical ores such as metamorphosed porphyry deposits of Proterozoic age, stratiform copper deposits hosted in sandstone, and fractionation mechanisms in S-type granitoids. These examples point to the fact that exploration should not be constrained by geologic didactics that exclude certain targets because of seemingly inappropriate lithology, tectonic setting, or epoch. Some of the great discoveries of the past have been made by thinking intuitively and "out of the box." Section II presents a variety of techniques that expand the armory of exploration tools available to the geoscientist: from microscopic and laboratory techniques involving mineral cathodoluminescence and isotope vectoring, to big data approaches aimed at geophysically imaging the Earth's crust. Although this book covers but a small fraction of the advances currently being made in mineral exploration science, it is timely because these innovations will catalyze the implementation of resource utilization policies that will, in the future, be more sustainable and environmentally responsive than at any time in the past.

**Sophie Decrée**
Royal Belgium Institute of Natural Sciences
and
Geological Survey of Belgium

**Laurence Robb**
University of Oxford
and
CIMERA – University of the Witwatersrand/
University of Johannesburg

# Section I
# Characteristics of Atypical Mineral Deposit Styles

# 1

# Origin and Exploration of the Kola PGE-bearing Province: New Constraints from Geochronology

**Felix P. Mitrofanov[1], Tamara B. Bayanova[1], John N. Ludden[2], Alexey U. Korchagin[1,3], Victor V. Chashchin[1], Lyudmila I. Nerovich[1], Pavel A. Serov[1], Alexander F. Mitrofanov[4], and Dmitry V. Zhirov[1]**

## ABSTRACT

The NE Fennoscandian Shield comprises the Northern (Kola) Belt in Finland and the Southern Belt in Karelia. The belts host mafic-ultramafic layered Cu-Ni-Cr and Pt-Pd-bearing intrusions. They were studied using precise isotope analyses with U-Pb on zircon and baddeleyite and Sm-Nd on rock-forming silicates and sulfides. The analyses indicate the 130 Ma magmatic evolution with major events at 2.53, 2.50, 2.45, and 2.40 Ga. It is considered to be governed by the long-lived mantle plume activity. Barren phases were dated at 2.53 Ga for orthopyroxenites and olivine gabbro in the Fedorovo-Pansky massif. Main PGE-bearing phases of gabbronorite (Mt. Generalskaya), norite (Monchepluton), and gabbronorites (Fedorovo-Pansky and Monchetundra massifs) yielded ages of 2.50 Ga. Anorthosites of Mt. Generalskaya, the Fedorovo-Pansky and Monchetundra massifs occurred at the 2.45 Ga PGE-bearing phase. According to regional geochronological correlations, this widespread event emplaced layered PGE-bearing intrusions of Finland (Penikat, Kemi, Koitelainen) and mafic intrusions in Karelia. Dikes of the final mafic magmatic pulse at 2.40 Ga are present in the Imandra lopolith. Slightly negative εNd values and ISr values of 0.703–0.704 suggest the layered intrusions to originate from an enriched EM-1-like mantle reservoir.

## 1.1. INTRODUCTION

Magmatic sulfide Ni-Cu-PGE and low-sulfide Pd-Pt deposits are best-valued commercial types of the Pd-Pt mineralization. In Russia, there is a well-known Ni-Cu-PGE deposit in Norilsk and a low-sulfide Pd-Pt deposit at the Monchegorsk and Fedorovo-Pansky massifs (Sluzhenikin et al., 1994). These deposits differ by their PGE mineralization. In the sulfide type, PGEs are accompanying components, and ferrous metals play the lead role, whereas in the low-sulfide type, Pd, Pt, and Rh are major, while nonferrous metals are secondary. Dividing PGE ores into the sulfide and low-sulfide types (groups) provides a basis for the classification proposed in Naldrett (2003), Dodin et al. (2001), and Likhachyov (2006).

In the 21st century, up to 90% of the platinum-group metals (PGM) production was related to processing of the Norilsk high-grade Ni-Cu-PGE ore. PGE were by-products, though in 2000–2001, their contribution to the price structure in the world's market was about 50%. According to Russian and American specialists (Dodin et al., 2001), the PGE production in Russia will be mainly related to mining of low-sulfide ores. Its resources in the Norilsk district are estimated at thousands of tons (Starostin & Sorokhtin, 2010). In contrast, PGE resources of the Kola region are estimated at hundreds of tons as of 2010.

Though the Kola low-sulfide PGE ores are a minor source of PGE in the global scope, they are widespread in the Kola region and require a detailed study (Mitrofanov

[1] *Geological Institute, Kola Science Centre, Russian Academy of Sciences (GI KSC RAS), Apatity, Russia*
[2] *British Geological Survey, Keyworth, Nottingham, UK*
[3] *JSC "Pana", Apatity, Russia*
[4] *SRK Consulting, Toronto, Canada*

*Ore Deposits: Origin, Exploration, and Exploitation, Geophysical Monograph 242*, First Edition.
Edited by Sophie Decrée and Laurence Robb.
© 2019 American Geophysical Union. Published 2019 by John Wiley & Sons, Inc.

et al., 2013). This paper provides a comprehensive study of the age distribution in the layered complexes. As some of them are barren, the geochronology may be used as a guide to explore or at least to understand their mineralization and magmatic settings.

## 1.2. LIPS AND LOW-SULFIDE DEPOSITS: GEOLOGICAL SETTING

Large Igneous Provinces (LIPs) are considered as derivatives of deep mantle plumes (Campbell and Griffits, 1990). In addition to alkaline and komatiite LIPs, a special group of LIPs comprises mafic intraplate continental provinces (Bleeker & Ernst, 2006) and consists of rift-related thick sedimentary and volcanic sequences, dike swarms, and intrusions of mafic and ultramafic rocks.

Some researchers provide geological, geophysical, and geochemical evidence of links between LIPs and deep mantle plumes (Grachev, 2003; Pirajno, 2007; Bogatikov et al., 2010). The plumes are considered to be active in the Precambrian regions, although many of ancient geological and geophysical features of terrestrial structures cannot be detected. Nevertheless, several indicators of an ancient intracontinental mafic LIP can be proposed (Mitrofanov et al., 2013; Robb, 2008; Rundkvist et al., 2006; Smol'kin et al., 2009):

- widespread areas of rocks associated with deep gravity anomalies that were caused by a granulite-mafic layer at the base of the crust;
- a rift-related (anorogenic) assembly, discordant with older basement structures. It occurs as multiphase extensional faulting that controls the arrangement of grabens, volcanic belts, extended dike swarms, and radial intrusive bodies;
- long-term, multistage, and pulsatory tectonics and magmatism;
- breaks in sedimentation and related erosion;
- early manifestations of tholeiitic basaltic (trap), high-magnesian (boninite-like) and alkaline magmatism in domains with the continental crust; formation of leucogabbro-anorthosite complexes;
- sills, lopoliths, sheetlike intrusions, large dikes, and dike swarms;
- multiphase and layered intrusions that differ from spreading and subduction-related rocks by geochemistry (Bleeker & Ernst, 2006). They have fine-scale fractionation (layering) and minor intermediate and felsic rocks, often with final leucogabbro and anorthosite and abundant pegmatoid mafic varieties;
- characteristic undepleted mantle geochemistry of rocks and ores with anomalously high contents of siderophile-chalcophile elements and LILE marked by $^{143}Nd/^{144}Nd$, $^{87}Sr/^{86}Sr$, $^{187}Os/^{188}Os$, and $^{3}He/^{4}He$ isotope ratios;
- large orthomagmatic Cr, Ni, Cu, Co, PGE ± Au, Ti, and V deposits.

The eastern Baltic (Fennoscandian) Shield hosts the vast Palaeoproterozoic East Scandinavian mafic LIP. Its current remnants cover about 1 mln km$^2$. The shield basement formed as a mature Archaean granulite and gneiss-migmatite crust 2550 Ma ago. It is exposed in the Kola-Lapland-Karelia Craton. Main structural features of the East Scandinavian mafic LIP and its Pd-Pt and Ni-Cu-PGE deposits are described in Mitrofanov et al. (2013). According to geophysical data, the lower crust in the eastern part of the shield is composed of a transitional crust-mantle layer ($Vp$ = 7.1–7.7 km/s). Deep xenoliths of granulites and garnet anorthosite are dated ~2460 Ma. They were taken out from this layer by the Kandalaksha explosion pipes. Compositionally, these rocks are close to the bodies exposed at the surface (Verba et al., 2005). It implies that masses of deep magma did not only ascend as volcanic rocks, dikes, and intrusions, but also underplated the crust (Mitrofanov, 2005). The exposed part of the shield extends beneath the sedimentary cover toward the northern Russian Platform as a vast Palaeoproterozoic Baltic-Mid-Russia wide arc-intracontinental orogen (Mints, 2011).

The geological map of the Fennoscandian Shield (2005) clearly shows the anorogenic pattern of grabens, dike swarms, and belts (trends) of intrusive bodies independent of the Archaean gneiss-migmatite framework. These intrusions, related deposits, and occurrences make up extended belts in the northern part of the province: the NW-trending Kola Belt and the NE-trending Karelian Belt with a concentration of intrusions in the Monchegorsk ore cluster (Fig. 1.1) (Bayanova et al., 2009).

The long Early Palaeoproterozoic (2530–2400 Ma) geological history of the East Scandinavian Mafic LIP (ESMLIP) comprises several stages. They are separated by breaks in sedimentation and magmatic activity often marked by uplift erosion and deposition of conglomerates. The Sumian stage (2550–2400 Ma) is crucial for the metallogeny of Pd-Pt ores. It can be related to the emplacement of high-Mg and high-Si boninite-like and anorthosite magmas (Mitrofanov, 2005; Sharkov, 2006). The ore-bearing intrusions were emplaced in the Kola Belt (Fedorovo-Pansky and other intrusions, 2530–2450 Ma) and in the Fenno-Karelian Belt (2450–2400 Ma) (Bayanova et al., 2009).

Recently, the Baltic Shield has been defined as the PGE-bearing ESMLIP of plume nature (Bayanova et al., 2009), or the Baltic LIP with igneous rocks rich in Mg and Si (Bogatikov et al., 2010), or the Kola-Lapland-Karelian plume province (Smol'kin et al., 2009). These Early Palaeoproterozoic geological settings fill a substantial gap in understanding of geological events and Pd-Pt and Ni-Cu metallogeny of the Late Neoarchaean-Early Palaeoproterozoic transitional period in the Earth's evolution (2.7–2.2 Ga ago). In classic metallogenic summaries (Naldrett, 2003; Groves et al., 2005), this period is characterized by the Stillwater, Great Dike of Zimbabwe, Bushveld, and Sudbury ore-bearing complexes. However,

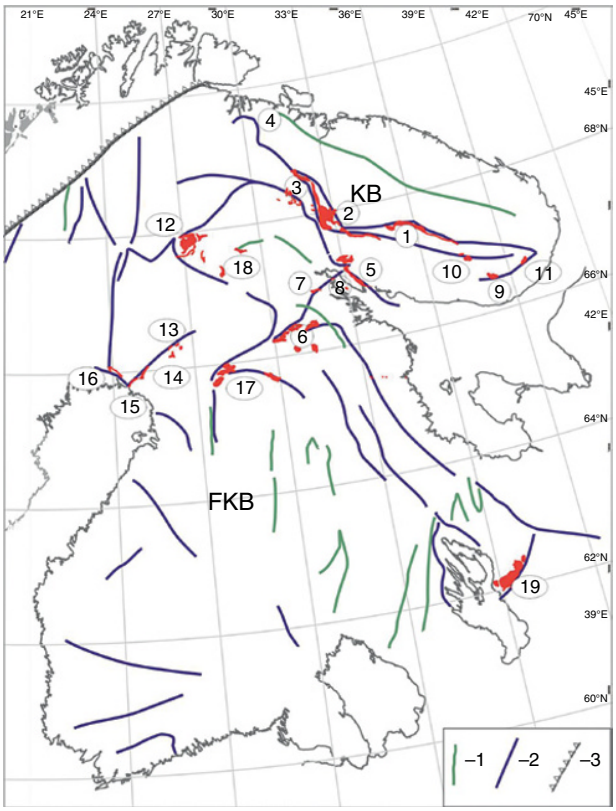


**Figure 1.1** Rift belts and known Paleoproterozoic mafic complexes in northern ESMLIP. KB, Kola Belt; FKB, Fenno-Karelian Belt. 1 - Archean belts; 2 - Paleoproterozoic belts; 3 - Thrust caledonides. Main layered complexes (numerals in figure): 1, Fedorov Pana; 2, Monchepluton; 3, Monchetundra, Volchetundra, gabbro of the Main Range; 4, Mt. General'skaya; 5, Kandalaksha and Kolvitsa intrusions; 6, Lukkulaisvaara; 7, Kondozero massif; 8, Tolstik; 9, Ondomozero; 10, Pesochny; 11, Pyalochny; 12, Keivitsa; 13, Portimo Complex (Kontijarvi, Siikakama, Ahmavaara); 14, Penikat; 15, Kemi; 16, Tornio; 17, Koillismaa Complex; 18, Akanvaara; 19, Birakov-Aganozero massif. Hundreds of intrusive bodies are out of scale (Mitrofanov et al., 2013).

their geological setting cannot be coordinated in space and time with regional geological frameworks.

The Neoarchaean and Palaeoproterozoic deposits (2.7–2.5 and 2.0–1.9 Ga) host the world's main resources of Pd-Pt ores in layered intrusions (~60 kt). Neoarchaean komatiites, Mesoproterozoic, and Late Paleozoic deposits contain Ni ores (Groves et al., 2005). These epochs coincide with the existence of the thick (250–150 km) continental lithosphere, completion of collision, and ascent of superplumes that developed over more than 200 Ma (Condie, 2004). The structures that host low-sulfide Pd-Pt deposits were typically within-plate (Groves et al., 2005).

Thus, recent studies of global geodynamics and metallogeny emphasize the importance of the period in the Earth's evolution 2.7–2.2 Ga ago, when the Neoarchaean to Palaeoproterozoic plume tectonics gave way to plate tectonics. It is particularly evident for the Kaapvaal and East European cratons (Glikson, 2014).

## 1.3. ANALYTICAL PROCEDURES, ISOTOPE U-PB METHOD

### 1.3.1. U-Pb (TIMS) Method with $^{208}Pb/^{235}U$ Tracer

The method proposed by Krogh (Krogh, 1973) was used to dissolve samples in strong (48%) hydrofluoric acid at a temperature of 205–210 °C over 1–10 days. In order to dissolve fluorides, the samples were reacted with 3.1 N HCl at a temperature of 130 °C for 8–10 hours. To determine the isotope composition of lead and concentrations of Pb and U, a sample was divided into two aliquots in 3.1 N HCl, then a mixed $^{208}Pb/^{235}U$ tracer was added. Pb and U were separated on an AG 1 × 8, 200–400 mesh anion exchanger in Teflon columns. A laboratory blank for the whole analysis was < 0.1–0.08 ng for Pb and 0.01–0.04 ng for U. All isotope determinations for zircon and baddeleyite were made on Finnigan MAT-262 and MI 1201-T mass spectrometers. The Pb isotope composition was analyzed on a secondary-ion multiplier on a Finnigan MAT-262 in an ion-counting mode. Measurements of the Pb isotope composition are accurate to 0.025% (Finnigan MAT-262) and 0.15% (MI 1201-T) when calibrated against NBS SRM-981 and SRM-982 standards, respectively. U and Pb concentrations were measured in a single filament mode with $H_3PO_4$ and silica gel added. The method described in Scharer and Gower (1988) and Scharer et al. (1996) was used. Pb and U concentrations were measured in temperature ranges of 1350–1450°C and 1450–1550°C, respectively. Isotope ratios were corrected for mass discrimination during static processing of replicate analyses of the SRM-981 and SRM-982 standards (0.12 ± 0.04% for the Finnigan MAT-262 and 0.17 ± 0.05% per a.m.u.). Errors in the U-Pb ratios were calculated during the statistical treatment of replicate analyses of the IGFM-87 standard. They were assumed equal to 0.5% for Finnigan MAT-262 and 0.7% for MI 1201-T. Isochrons and sample points were calculated using the Squid and Isoplot programs (Ludwig, 1991, 1999). Age values were calculated with the conventional decay constants for U (Steiger & Jager, 1977). All errors are reported for a 2-sigma level. Corrections for common Pb were made according to Stacey and Kramers (1975). Corrections were also made for the composition of Pb separated from syngenetic plagioclase or microcline, if the admixture of common Pb was >10% of the overall Pb concentration and the $^{206}Pb/^{204}Pb$ ratios were <1000.

### 1.3.2. $^{205}Pb/^{235}U$ Tracer for Single Grains

The U-Pb (TIMS) method was based on the U-Pb method for single grain accessory minerals using ion-exchange chromatography (Corfu et al., 2011). Handpicked crystals are first treated in ultrasonic bath for cleaning in spirit or in acetone, and then in 7 N nitric acid. Then they are heated for about 15 minutes on a

warm rangette and are finally flushed three times with recurrent purification water. Chemical mineral decomposition is performed in Teflon bombs, adding 3 to 5 mcl of mixed $^{205}Pb/^{235}U$ tracer in concentrated nitric acid during 5 to 7 days at a temperature of 210°C. The technique is provided in Krogh (1973). After the complete decomposition, the column effluent is evaporated on a warm rangette. Then 10 drops of 6.2 N chlorohydric acid are added. The sample is placed to the thermostat for 8 to 10 hours at a temperature of 140–150°C for homogenization. Pb and U are separated using ion-exchange chromatography in columns with Dowex IX8 200–400 mesh resin. Pb is eluted with 10 drops of 6.2 N chlorohydric acid, when one drop of 0.1 N phosphoric acid is added and the solution is evaporated on a rangette down to 3 mcl. U is eluted separately from Pb, when 20 drops of water with one drop of 0.1 N phosphoric acid are added. It is evaporated on a rangette down to 3 mcl. All chemical procedures are performed in an ultraclean block with blank Pb and U contamination of ca.1–3 pg and ca.10–15 pg, respectively. Pb and U isotope composition and concentrations are measured on Re bands at seven-channel mass-spectrometer Finnigan-MAT 262 (RPG), on collectors, with $^{204}Pb$ and $^{205}Pb$ measured at a temperature of 1350–1450°C in an ion-counting mode using a multiplier or quadrupole RPG accessory. Silica gel is used as an emitter. U concentrations are detected at a temperature of 1450–1550°C using a collector and a multiplier in a mixed statically dynamic mode. When U concentrations are negligible, a multiplier or quadrupole RPQ accessory is applied in a dynamic mode. All the measured isotope ratios are adjusted for the obtained mass-discrimination, when parallel analyses of SRM-981 are studied and SRM-982 standards are 0.12 ± 0.04%. Coordinates of points and isochrone parameters are calculated according to Ludwig (1991, 1999). Ages are calculated in accordance with the accepted values of U decay constants (Steiger & Jager, 1977), with errors indicated on a 2b level. The Stacey and Kramers model is used to adjust numbers for the admixture of common Pb (Stacey & Kramers, 1975).

### 1.3.3. Isotope Sm/Nd Method

In order to define concentrations of Sm and Nd, a sample was mixed with a compound tracer $^{149}Sm/^{150}Nd$ prior to dissolution. It was then diluted with a mixture of $HF + HNO_3$ (or + $HClO_4$) in Teflon sample bottles at a temperature of 100°C until complete dissolution. Sm and Nd were extracted by standard procedures with a two-stage ion-exchange and an extraction-chromatographic separation. An ion-exchange tar Dowex 50 × 8 in chromatographic columns employing 2.3 N and 4.5 N HCl was used as an eluent. The separated Sm and Nd fractions were transferred into nitrate form, whereupon the samples (preparations) were ready for mass-spectrometric analysis. Nd-isotope composition and Sm and Nd concentrations were measured by isotope dilution. A multicollector mass-spectrometer in a Finnigan MAT 262 (RPQ) was used in a static mode with Re + Re and Ta + Re filament. The reproducibility measured for ten parallel analyses of the Nd-isotope composition (standard La Jolla = 0.511833 ± 6) was <0.0024% (2σ). The same reproducibility was obtained from 11 parallel analyses of the Japanese standard: Ji Nd1 = 0.512078 ± 5. The error in $^{147}Sm/^{144}Nd$ ratios of 0.2% (2σ), the average of seven measures, was accepted for statistic calculations of the Sm and Nd concentrations using the BCR standard. Blanks for laboratory contamination for Nd and Sm were 0.3 and 0.06 ng, respectively. Isochron parameters were developed from programs made by Ludwig (Ludwig, 1991 and 1999). The reproducibility of measurements was ± 0.2% (2σ) for Sm/Nd ratios and ± 0.003% (2σ) for Nd-isotope analyses. All $^{147}Sm/^{144}Nd$ and $^{143}Nd/^{144}Nd$ ratios were normalized to $^{146}Nd/^{144}Nd = 0.7219$ and adjusted to $^{143}Nd/^{144}Nd = 0.511860$ using the La Jolla Nd standard. The εNd (T) values and model TDM ages were calculated based on the currently accepted parameters of CHUR (Jacobsen & Wasserburg, 1984): $^{143}Nd/^{144}Nd = 0.512638$ and $^{147}Sm/^{144}Nd = 0.1967$ and DM (Goldstein and Jacobsen, 1988): $^{143}Nd/^{144}Nd = 0.513151$ and $^{147}Sm/^{144}Nd = 0.2136$.

Sulfide minerals (pyrite, pentlandite, chalcopyrite, etc.) were chemically and analytically treated for the Sm-Nd study following a modified (Ekimova et al., 2011) conventional technique (Zhuravlyov et al., 1987). To decompose sulfides, a mineral weight (20 to 50 mg) is mixed with a $^{149}Sm/^{150}Nd$ tracer solution, treated with aqua regia ($HCl + HNO_3$) until complete decomposition and evaporated dry. Afterwards, it is converted to chlorides through evaporating the sample in 4.5–6 N HCl. After the fractional acid decomposition, the dry residue is dissolved in ~1ml 2.3 N HCl. Then REEs are separated from the solution via cation-exchange chromatography. A stepwise elution method is applied to 2.3 and 4.5 N HCl in a chromatographic column with cation-exchange resin Dowex 50 × 8 (200–400 mesh). The separated REE fraction is evaporated dry, dissolved in 0.1 N HCl and loaded to the second column with KEL-F solid ion-exchange resin HDEHP. The resin is used to separate Sm and Nd. The selected Sm and Nd fractions are evaporated to get prepared for further mass-spectrometric analysis. The Nd isotope composition and Sm and Nd concentrations were measured by an isotope dilution technique. A 7-channel solid-phase mass-spectrometer Finnigan-MAT 262 (RPQ) was used in a static double-band mode in collectors with Ta + Re filaments. Re filaments were used as ionizers. A sample was applied to a Ta filament with a diluted $H_3PO_4$ microdrop. The reproducibility error for 11 determinations of the Nd isotope composition of La Jolla = 0.511833 ± 6 (2σ, N = 11) was up to 0.0024% (2σ).

The same error was obtained for 44 parallel analyses of a new Japanese standard, JNdi1 = 0.512072 ± 2 (2σ, N = 44). The error in $^{147}Sm/^{144}Nd$ ratios is accepted for static calculations of the Sm and Nd concentrations in BCR-1 to be 0.2% (2σ). It is an average of 7 measurements. The blank intralaboratory contamination in Nd and Sm is 0.3 ng and 0.06 ng, respectively. The measured Nd isotope rations were normalized per $^{148}Nd/^{144}Nd = 0.241570$ and recalculated for $^{143}Nd/^{144}Nd$ in La Jolla = 0.511860 afterward. The isochron parameters were computed using programs of K. Ludwig (Ludwig, 1991, 1999). Decompositions constants are as per Steiger & Jager (1977). εNd parameters were calculated according to DePaolo (1981) for a one-stage model and according to Liew and Hofmann (1988) for a two-stage model.

### 1.3.4. Isotope Rb/Sr Method

The samples and minerals were all treated with double distilled acids (HCl, HF, and $HNO_3$) and $H_2O$ distillate. A sample of 20–100 mg (depending on Rb and Sr contents) was dissolved with 4 ml of mixed HF and $HNO_3$ (5:1) in corked Teflon sample bottles and left at a temperature of about 200°C for one day. The solution was then divided into three aliquots in order to determine Rb and Sr isotope compositions and concentrations. These were measured by isotope dilution using separate $^{85}Rb$ and $^{84}Sr$ tracers. Rb and Sr extraction was performed by eluent chromatography with Dowex tar 50 × 8 (200–400 mesh). 1.5 N and 2.3 N HCl served as an eluent. Tar volumes in the columns were c. 7 and c. 4 $cm^3$. The separated Rb and Sr fractions were evaporated until dryness, followed by treatment with a few drops of $HNO_3$. Sr isotope compositions and Rb and Sr contents were measured by a MI-1201-T (Ukraine) mass spectrometer in the two-ribbon mode with Re filaments. The samples were deposited on the ribbons in the form of nitrate. Sr isotope composition in the measured samples was normalized to a value of 0.710235 recommended by NBS SRM-987. Errors on Sr isotope analysis (confidence interval of 95%) are up to 0.04%, and those of Rb-Sr ratio determination are 1.5%. Blank laboratory contamination for Rb is 2.5 ng and for Sr 1.2 ng. The adopted Rb decay constant of Steiger & Jager (1977) was used for age calculations.

### 1.3.5. Isotope Re/Os Method

The isotope analysis of sulfides has been provided in VSEGEI (Saint-Petersburg). The method of Re and Os chemical extraction described in Birck et al. (1997) has been applied. Samples of minerals with the weight of 50–200 mg were dissociated in a mixture of reagents (1 ml Br2 + 2 ml 7 N HNO3 + 0.5 ml 40% CrO3 in 7 N HNO3) in 5-ml Teflon Savillex vials under the temperature of 90 °C for 48 hours. After that Os was extracted using the microdistillation method. Re was extracted by liquid extraction with the isoamyl alcohol. The isotope dilution method with the mixed tracer $^{185}Re/^{190}Os$ was used to define the Re and Os concentrations and $^{187}Re/^{188}Os$ ratio. The tracer was added until samples were dissociated. Os as bromides was applied on a Pt filament with 0.2 ml of emitter $Ba(OH)_2 + NaOH$. The Os isotope composition was measured with the Triton (Thermo Scientific) solid-phase multicollector mass-spectrometer using ion source in a dynamic mode in negative ions. The inner standard of $^{187}Os/^{188}Os$ is 0.11997 ± 0.00001. The Element-2 (Thermo Scientific) mass-spectrometer with the inductively coupled plasma was used to measure the Re isotope composition. Re was measured from the solution of 3% $HNO_3$ using a multiplier in a dynamic mode. A quartz nebulizer, Ni cones, and a peristaltic pump were used. The measurements were carried with an average resolution. The Re standard of 10 mg/t was measured in the beginning and in the end of a session. The obtained value was averaged and the correcting factor of the mass deviation was estimated. The analysis accuracy is 0.5%. The measured standard $^{185}Re/^{187}Re$ ratios are within the range of 0.585–0.591, with the table standard of 0.5974 (Gramlich et al., 1973).

### 1.3.6. Study of Sulfide Mineral Texture and REE

Sulfides were studied using back-scattered electrons with a high-performance LEO 1450 scanning electron microscope. Analyses were carried to study possible inclusions in sulfides with considerable concentrations of REE that might have distorted results of Sm-Nd dating (Elizarova et al., 2009).

To define REE in samples with no preliminary separation and concentration, reference values of REE concentrations in the GSO 2463 standard (apatite), sulfide from the Talnakh deposit, and international standard samples of the Centre of Petrographic and Geochemical Research (Nancy, France) were reproduced using the ELAN 9000 DRC-e (Perkin Elmer, USA) quadrupole mass-spectrometer in ICTREMRM KSC RAS, Apatity. The samples were separated under the conditions provided in Elizarova and Bayanova (2012).

### 1.3.7. LA-ICP-MS of PGE in Sulfides

To analyze concentrations of Cr, Co, As, Se, Ru, Rh, Pd, Ag, Cd, Sb, Re, Os, Ir, Pt, Au, Tl, Pb, and Bi in sulfides, laser ablation (UP-213 laser) was used on a high-resolution Element-XR mass spectrometer with ionization in an inductively coupled plasma LA-ICP-MS. Measurement parameters were as follows: 40 μm crater diameter, 4 Hz impulse frequency of laser radiation. Samples were analyzed by blocks. They were prepared

using the Element XR software with measurement of standard samples in the beginning and in the end of each block. Internal laboratory sulfide standards were used for analysis. The deviation defined from calibration standards is +−10 – 20%. Fe abundance was applied as an internal standard, since (a) its concentrations are high in relation to background values and (b) it occurs in all studied samples being the most homogeneously distributed in phases. The data were processed using the Glitter software (Jackson, 2001).

## 1.4. FEDOROVO-PANSKY COMPLEX: GEOLOGICAL SETTING

The Fedorovo-Pansky Layered Complex (Fig. 1.2) exposes over an area of >400 km$^2$. It strikes northwestward for >60 km and dips southwestward at an angle of 30°–35°. The total rock sequence is about 3–4 km thick. Tectonic faults divide the complex into several blocks. The major blocks from west to east (Fig. 1.2) are known as the Fedorov, Lastjavr, Western, and Eastern Pansky (Mitrofanov, 2005). The Fedorovo-Pansky Complex is bordered by the Archaean Keivy terrain and the Palaeoproterozoic Imandra-Varzuga rift. The rocks of the complex crop out close to the Archaean gneisses only in the NW extremities, but their contacts cannot be defined because of their poor exposure. In the north, the complex borders alkaline granites of the White Tundra intrusion. The alkaline granites were proven to be Archaean with a U-Pb zircon age of 2654 ± 15 Ma (Bayanova, 2004; Zozulya et al., 2005). The contact of the Western Pansky Block with the Imandra-Varzuga volcano-sedimentary sequence is mostly covered by Quaternary deposits. However, drilling and excavations to the south of Mt. Kamennik reveal a strongly sheared and metamorphosed contact between the intrusion and overlying Palaeoproterozoic volcano-sedimentary rocks that we consider to be tectonic.

The Fedorovo-Pansky Complex mostly comprises gabbronorites with varying proportions of mafic minerals and different structural features (Fig. 1.3). From the bottom up, the layered sequence is as follows:

- Marginal Zone (50–100 m) of plagioclase-amphibole schists with relicts of massive finegrained norite and gabbronorite, which are referred to as chilled margin rocks;
- Taxitic Zone (30–300 m), which contains an ore-bearing gabbronoritic matrix (2485 Ma) and early xenoliths of plagioclase-bearing pyroxenite and norite (2526–2516 Ma). Syngenetic and magmatic ores are represented by Cu and Ni sulfides with Pt, Pd, and Au,

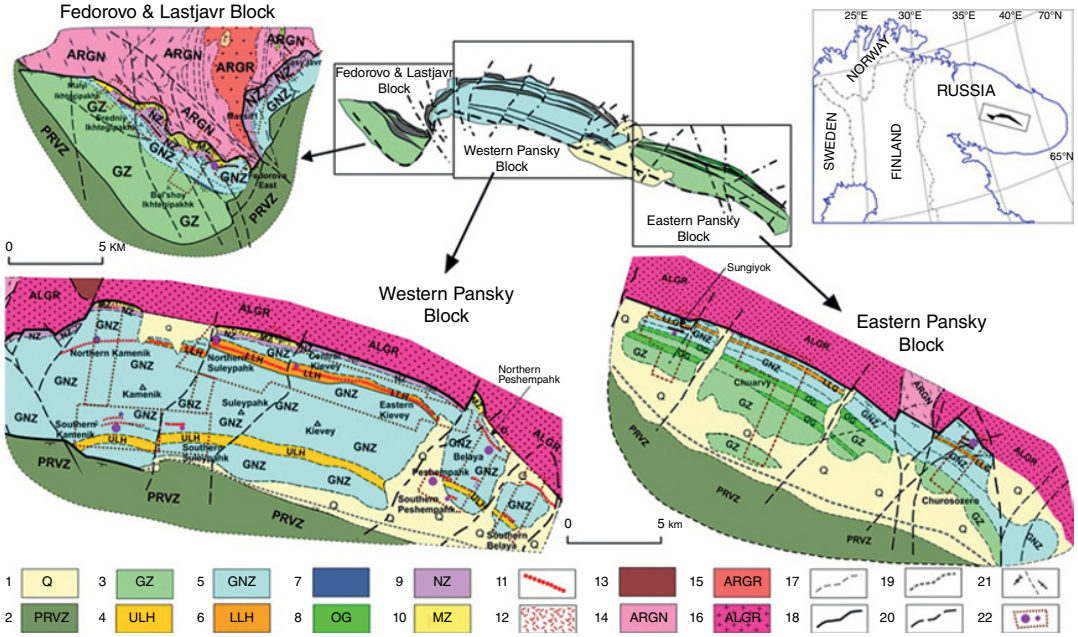


**Figure 1.2** General geological map of the Fedorovo-Pansky Layered Complex. (1) Quaternary deposits; (2) The Imandra-Varzuga Proterozoic volcano-sedimentary complex; (3) Gabbro Zone; (4) Upper Layered Horizon; (5) Gabbronorite Zone; (6) Lower Layered Horizon; (7) Alternating gabbro, gabbrnorite and troctolite; (8) Olivine gabbro and gabbronorite horizons; (9) Norite Zone; (10) Marginal Zone – Mafic schists; (11) PGE reef-type mineralization; (12) PGE contact-type mineralization; (13) Early Proterozoic Tsaga gabbro-anorthosite massif; (14) Archaean Kola gneiss; (15) Archaean plagiomicrocline granite; (16) Archaean Keivy alkaline granite; (17) Boundaries between geological units; (18) Reliable boundaries between rock complexes with different ages; (19) Assumed boundaries between rock complexes with different ages; (20) Tectonic dislocations; (21) Schistosity, gneissic banding; (22) Boundaries of license areas with titles of deposits (large circles) or prospects (small circles) (Mitrofanov et al., 2005).

as well as Pt and Pd sulfides, bismuth-tellurides, and arsenides;

• Norite Zone (50–200 m) with cumulus interlayers of harzburgite and plagioclase-bearing pyroxenite that includes an intergranular injection Cu-Ni-PGE mineralization in the lower part. The rocks of the zone are enriched in chromium (up to 1000 ppm) and contain chromite. It is also typical of the rocks of the Penikat and Kemi intrusions (Finland) derived from the earliest magma portion (Iljina & Hanski, 2005). Basal Cu-Ni-PGE deposits of the Fedorov Block were explored and prepared for licensing (Schlissel et al., 2002; Mitrofanov et al., 2005).

• Main Gabbronorite Zone (c. 1000 m) is a thickly layered "stratified" rock series (Fig. 1.3) with a 40–80 m thinly layered lower horizon (LLH) at the upper part.

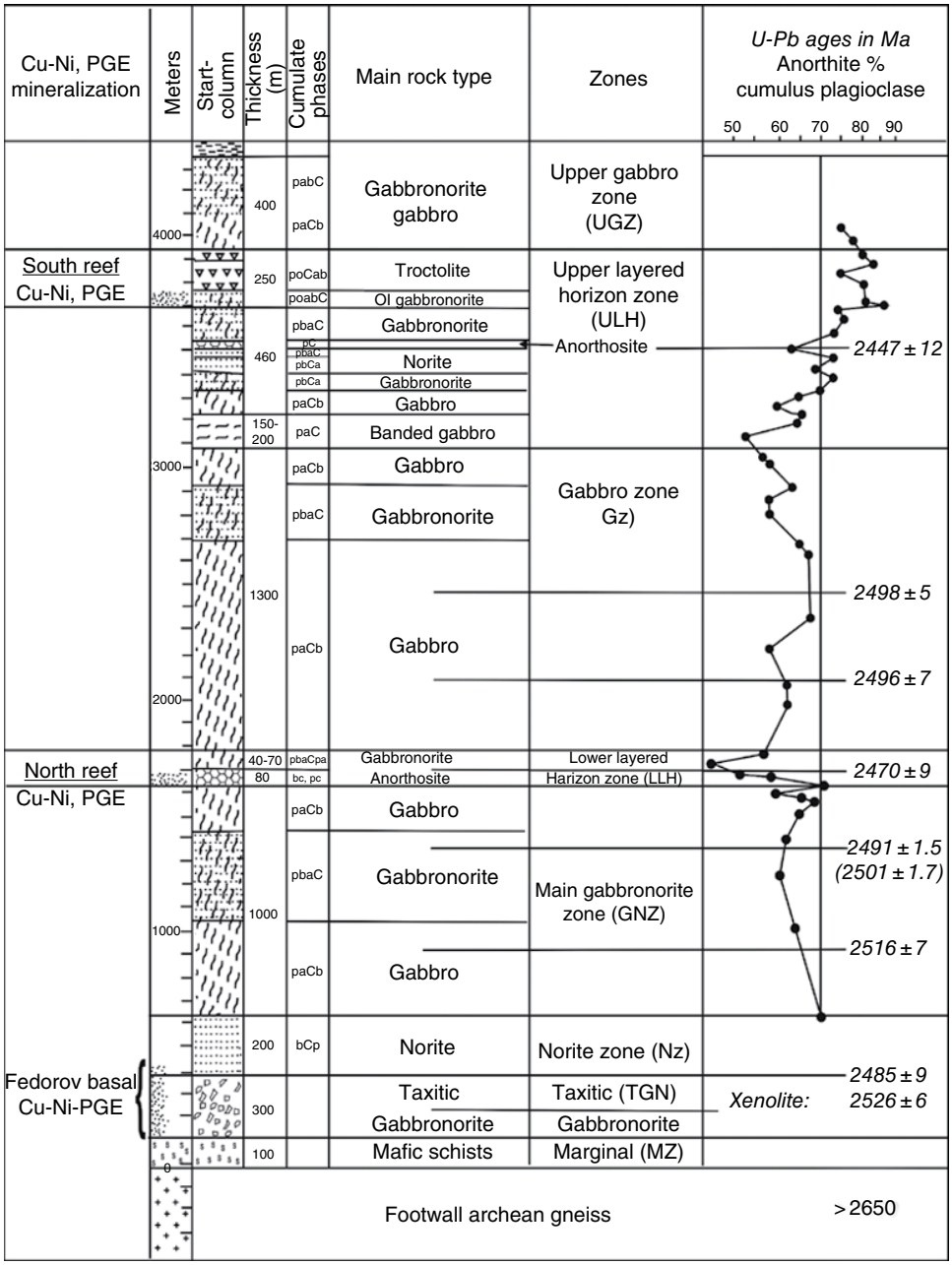


**Figure 1.3** Composite "stratigraphic" section of the Fedorovo-Pansky Complex with Cu-Ni and PGE mineralization (modified after Schissel et al., 2002). The cumulate mineral terminology used in this paper is that of cumulate phase minerals in small letters, in order of volume percent, preceding the capital C for cumulate, with postcumulate mineral phases following. Major mineral abbreviations are a = augite; b = bronzite; c = chromite; o = olivine; p = plagioclase (see Table 1.5 for references). Modified after Schissel et al., 2002.

LLH consists of contrasting alteration of gabbronorite, norite, pyroxenite, and interlayers of leucocratic gabbro and anorthosite. LLH contains a reef-type PGE deposit poor in base-metal sulfides. According to field investigations (Latypov & Chistyakova 2000), LLH anorthositic layers intruded later, as shown by cutting injection contacts. It is confirmed by a zircon U-Pb age for the anorthosite of 2470 ± 9 Ma.

• Upper layered horizon (ULH) between the Lower and Upper Gabbro Zones. ULH consists of olivine-bearing troctolite, norite, gabbronorite, and anorthosite (Fig. 1.3). It comprises several layers of rich PGE (Pd **S>** Pt) ore poor in base-metal sulfides (Mitrofanov et al., 2005). The U-Pb age of the ULH rocks on zircon and baddeleyite is 2447 ± 12 Ma (see below). It is the youngest among those obtained for the Fedorovo-Pansky Complex rocks (Bayanova, 2006; Bayanova et al., 2017).

## 1.5. MONCHEPLUTON ORE COMPLEX: GEOLOGICAL SETTING

The NE Fennoscandian Shield hosts two large Palaeoproterozoic layered intrusions in its central part, that is, the Monchegorsk (Fig. 1.4) mafic-ultramafic pluton (Monchepluton, 55 $km^2$) and the substantially mafic Monchetundra massif (120 $km^2$). They compose the Monchegorsk Complex of layered intrusions (Sharkov, 2006; Sharkov & Chistyakov, 2014; Konnikov & Orsoev 1991; Grokhovskaya et al., 2012) and are incorporated into the Monchegorsk Cr-PGE-Cu-Ni ore district (Korovkin et al., 2003).

The ore potential of the Monchegorsk area is mainly provided by deposits of the Monchepluton. It is one of the most productive plutons among numerous Palaeoproterozoic layered intrusions of the Fennoscandian Shield. There is a series of ore deposits and occurrences related to the pluton in space and origin. Initially, the study of the Monchepluton was focused on complex Ni-Cu-PGE syn- and epigenetic ores. They have been an ore source for the Severonikel Plant for a long time. In the late twentieth century, the large Sopcheozero chrome deposit was discovered by Grokhovskaya et al. (2000) and explored by Chashchin et al. (1999). At the same time, Grokhovskaya et al. (2000), and Ivanchenko (2008, 2009) studied the Monchepluton (Vurechuayvench and Horizon 330 of the Sopcha massif), as well as its southern framing (South Sopcha). The study resulted in the discovery of low-sulfide Pt-Pd ores. It allows us to consider the Monchegorsk area as a large-scale source of Cr, Ni-Cu-PGE, and Pt-Pd ores.

The geochronological data on the Monchetundra massif are clustered into two groups. The first group comprises isotope results on medium-grained mesocratic gabbronorite from the middle part of the massif (2505–2501 Ma) (Mitrofanov & Smol'kin, 2004; Bayanova, 2004). The second group provides isotope results on coarse-grained leucogabbro and leucogabbronorite from the upper part of the massif (2476–2453 Ma) (Mitrofanov et al., 1993; Nerovich et al., 2009; Bayanova et al., 2010). The significantly different ages show that either the massif consists of several intrusive phases, or it was formed over a long time.

Despite numerous geochronological studies of the Monchepluton and Monchetundra, there is still a number of questions to be answered. The most important of these are (a) the age of Pt-Pd reefs and basal ores and (b) the source of the ore matter. The current paper provides a comprehensive study of these issues. Their solution is approached via direct timing of the PGE ore formation using Sm-Nd isotope analysis of sulfide minerals that compose Pt-Pd ores (Serov et al., 2014). We present new results of isotope geochronological U-Pb and Sm-Nd analyses of the low-sulfide PGE mineralization and the Monchepluton host rocks. The study focuses on the critical horizon at the Nyud-II deposit, Horizon 330 of Mt. Sopcha, Vurechuaivench deposit, and massifs from the southern part of the Monchetundra (South Sopcha deposit) and Lake Moroshkovoye.

## 1.6. MONCHEPLUTON AND ITS SOUTHERN FRAMEWORK

The Monchepluton is located in the central Kola Peninsula at the NW edge of the Palaeoproterozoic Imandra-Varzuga volcanic-sedimentary rift structure. Currently, the pluton is arc shaped and consists of two branches (chambers). The NW branch is more than 7 km in length and comprises the Nittis-Kumuzhya-Travyanaya (NKT) deposit. The nearly latitudinal branch is about 11 km in length and consists of the Sopcha-Nyud-Poaz and Vurechuayvench massifs (Fig. 1.4).

The pluton is differentiated in the vertical and horizontal directions, that is, the rocks become less basic from the bottom up and from west to east. Dunite, harzburgite, orthopyroxenites (NKT), orthopyroxenites (Sopcha), norites (Nyud), and gabbronorites (Poaz, Vurechuayvench) make up a common syngenetic series of rocks (Kozlov, 1973). In the upper part, a continuous orthopyroxenite body of the Sopcha massif is disturbed by Horizon 330. It is a sheetlike body (low-angle syncline), as thick as 1.2 to 14.8 m (3.5 m, on average), 3300 m in extent, and 1200 m wide (Fig. 1.4). Horizon 330 is considered to originate as an injection of an additional magma batch. It is more basic and has higher temperature than the initial melt in the magma chamber (Konnikov & Orsoev 1991; Mitrofanov & Smol'kin (eds) 2004; Sharkov & Chistyakov, 2014). The horizon is characterized by a rhythmic sequence of thin (10–130 cm) layers composed of dunites, harzburgites, olivine orthopyroxenites and feldspatic

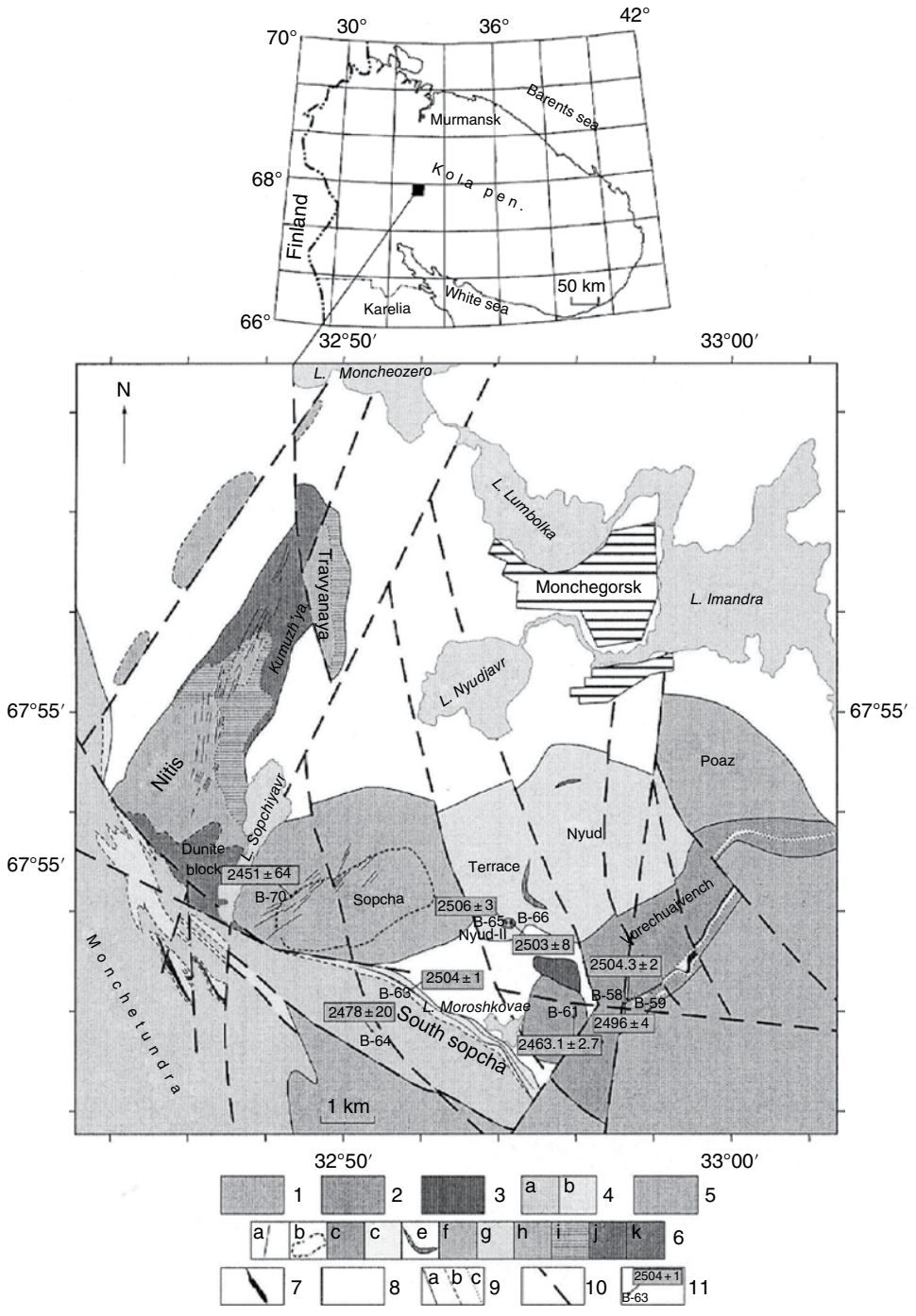


**Figure 1.4** Schematic geological map of Nyud massif and section along line I-I. (1) orthopyroxenites from Sopcha massif; (2–5) Nyud massif: (2) irregular alternation of microgabbronorites, micronorites, meso- and melanocratic norites, and plagiopyroxenites (critical horizon); (3) leuco- and mesocratic norites; (4) melanocratic olivine norites; (5) melanocratic norites with locally occurring plagiopyroxenites; (6) mesocratic gabbronorites of Poaz massif; (7) meso- and leucocratic metagabbronorites of Vurechuaivench massif; (8) quartz metagabbro of 10 anomaly massif; (9) Archean quartz diorites and gneissic diorites; (10) faults; (11) geological boundaries: (a) reliable, (b) inferred, and (c) facies; (12) location of geochronological samples and their numbers (after Chaschin et al., 2016).

orthopyroxenites (Kozlov, 1973; Konnikov & Orsoev 1991; Mitrofanov & Smol'kin, 2004). The layering is disturbed by bends and folds formed as a result of melt flow.

The critical horizon occurs in the middle of the Nyud massif section and consists of two parts called Terrace and Nyud-II. The Terrace critical horizon is up to 50 m thick (Fig. 1.4). It is composed of irregularly alternating meso- and melanocratic norites, plagioclase-bearing orthopyroxenites, gabbronorites, harzburgites, microgabbro, and microgabbronorites. The Nyud-II critical horizon is a stocklike body as big as 160 × 70 m. It has a convex bottom and a vertical thickness of about 50 m (Fig. 1.4). Melanocratic poikilitic norite is dominant in this critical horizon, along with mesocratic norites interlayers in the upper part and plagioharzburgites, olivine norites, plagioclase orthopyroxenites interlayers, minor bodies of pegmatoid leucocratic norites in the lower part. There are also isometric bodies of heterogeneous composition and structure. They are composed of fine-grained norites, gabbronorites, and hornfels among melanocratic and olivine norites (Bartenev & Dokuchaeva, 1975).

There are two concepts of the critical horizon origin: (a) it marks a roof of the earlier magma chamber overlain by a later chamber filled with norite-gabbronorites (Kozlov, 1973; Mitrofanov & Smol'kin, 2004), and (b) the critical horizon is an additional intrusive phase of the Monchepluton (Sharkov, 1982; Sharkov & Chistyakov, 2014).

Metagabbronorites and anorthosites of the Vurechuayvench massif occur in the SE Monchepluton at its contact with volcanic rocks of the Imandra-Varzuga riftogenic structure (Fig. 1.4). The massif occurs to the northeast of the Nyud-Poaz massifs and composes their section. Thus, it is the uppermost part of the whole Monchegorsk pluton section (Mitrofanov & Smol'kin, 2004). The Vurechuayvench massif is 1.5–2.0 km wide and 600–700 km thick. It stretches northeastward for 8 km. The massif is not inscribed into the general synformal structure of the Monchepluton, but dips to the southeast at angles of 5°–10° to 20°–30° beneath volcanic rocks of the Imandra-Varzuga structure. They overlie the massif with a 10 m-thick basal bed of residual conglobreccia (Gorbunov,1982). The section of the Vurechuayvench massif is represented by the following rock varieties (from the bottom up): bottom gabbronorites, 5–10 m thick, foliated and brecciated in the contact zone; continuous melano- and mesocratic norites (400–650 m); mesocratic metagabbronorites (300 m) with several metaplagioclasites horizons. The thickness of the latter varies from 10–15 to 40–50 m. This is a light grey rock with large spots containing up to 90–95 vol% of saussuritized and pelitized plagioclase with insignificant amounts of quartz and amphibole. The low-sulfide Pt-Pd ore deposit is spatially and genetically related to a metaplagioclasites horizon (Grokhovskaya et al., 2000).

Metagabbro intrusions of Anomaly 10, Lake Moroshkovoye and South Sopcha are situated in the southern extremity of the Monchepluton (Fig. 1.4). Anomaly 10 is an oval-shaped sheetlike metagabbro massif as big as 300 × 700 m in plan (Fig. 1.4). It is elongated in the latitudinal direction and sheetlike in section. The sheet dips to the northeast at an angle of 45° (Kozlov, 1973) and is composed of amphibolized fine- to coarse-grained leuco- and melanocratic quartz gabbro. Low-sulfide PGE and the associated oxide-sulfide mineralization occur at high levels of the massif near the contact with country diorite. At the bottom, there is a 500 m-long and 2 m-thick stratiform body.

The Lake Moroshkovoye massif occurs to the south of the Nyud massif and adjoins the SW flank of the Vurechuayvench massif. In the north, it contacts with metagabbro of the Anomaly 10 massif. In the west, SW and NW, the Lake Moroshkovoye massif cuts Archaean gneissic diorites (Fig. 1.4). The massif mainly consists of leuco- to mesocratic metanorites that give way to melanocratic metanorite and metagabbronorite in the marginal zone. The SW tectonic contact separates the massif from country gneissic diorites. The border is marked by a zone of shearing and foliation as thick as 5–10 to 35 m, gently dipping to the NE. It is represented by actinolite and actinolite-chlorite schists developed after gabbronorites. The quartz-chlorite schists after diorites contain sulfide mineralization and PGM.

The South Sopcha massif is about 5 km long and up to 1.5 km wide. It is oriented in the NW direction (Fig. 1.4). In the north, the massif borders a wide near-latitudinal tectonic zone of the Sopcha orthopyroxenites. In the NE, it contacts with Archaean gneissic diorites. In the south and SW, the South Sopcha massif is overlain by felsic metavolcanics of the Arvarench Formation in the Imandra-Varzuga structure along the tectonized intrusive contact. It is represented by fine-grained gabbro-amphibolites, up to 200 m thick. The age of the Arvarench Formation is 2429 ± 6.6 Ma (Vrevsky, 2011). In the NW, the South Sopcha massif passes a fault zone to the Monchetundra massif (Fig. 1.4). The South Sopcha massif has a monoclinal structure in section, dipping to the SW at angles of 5°–20° to 45°. It is affected by a large tectonic zone of the Monchetundra Fault, that is, the rocks are intensely foliated and altered.

The internal structure of the South Sopcha massif consists of a lower norite-orthopyroxenite zone and an upper gabbroic zone. The lower zone is 250–300 m thick. It is represented by an irregular alternation of metanorites and metapyroxenites interlayers, 1–20 m in thickness, with schlieren and bodies of pegmatoid rock varieties, irregular in shape, with a subordinate amount of metaperidotites.

Fresh rocks are extremely rare. As a rule, they are intensely amphibolized and saussuritized. The lower zone rocks host sulfide disseminations and pocketlike segregations with the low-sulfide PGE mineralization.

The upper zone of the South Sopcha massif is composed of leuco- to mesocratic coarse-grained mottled metagabbro and metagabbronorites. They are characterized by the constant occurrence of accessory titanomagnetite. These metagabbroic rocks are chemically close to those in the upper zone of Monchetundra massif (Grokhovskaya, 2012), but differ in their high-grade metamorphism and intense foliation, probably due to their thinning and localization in the tectonically active zone. The contact between the rocks of the lower and upper zones is mostly foliated and tectonized. Chlorite-actinolite schist interlayers occur in the lower zone. At the same time, there are sporadic bodies of magmatic breccia with fragments of metanorites and metapyroxenites from the lower zone and cement comparable to the metagabbroic rocks of the upper zone (Rundkvist et al., 2011). These relationships indicate that rocks various in composition are probably related to separate intrusive phases.

## 1.7. LOW-SULFIDE PGE DEPOSITS AND OCCURRENCES IN THE MONCHEGORSK ORE AREA

The low-sulfide Pt-Pd deposits and occurrences have been recently discovered throughout the Monchegorsk ore area (Chashchin et al., 2016). They are new for the Kola region and divided into two structural types: (1) stratiform reefs conformable to layering in massifs and (2) basal type bodies localized in marginal zones of intrusions. The first type is represented by the Vurechuayvench deposit, Horizon 330, and probably the critical horizon at the Nyud deposit. The second type is represented by the South Sopcha and the Lake Moroshkovoye deposits.

### 1.7.1. Vurechuayvench Deposit

The Vurechuayvench deposit is a low-sulfide Pt-Pd deposit of the reef type (Grokhovskaya et al., 2000). It is clearly stratiform and related to the anorthosite horizon. The ~2 km-long ore zone consists of several sheetlike and lenticular ore bodies up to 3 m thick and up to 300–500 m long. They are conformable to the massif layering and gently dip to the SE at angles of 2°–5° to 10°–15° (Grokhovskaya et al., 2000). The ore bodies have no distinct borders. Their boundaries are established only by sampling results. The PGE mineralization is closely associated with sulfide disseminations. They develop nonuniformly from 1–2 mm-big sporadic segregations with sulfide contents of about 1 vol% to 1–5 mm-big pockets (2–3 vol%) and sulfide schlieren (5–10 vol%). Sulfides are mainly represented by chalcopyrite (40–90 vol%) and millerite (10–50 vol%) with subordinate amounts of covellite, chalcocite, pentlandite, pyrrhotite, and pyrite. There are nickel sulfoarsenides (gersdorffite) and cobalt sulfoarsenides (cobaltite) as well. PGM are represented by bismuthotellurides (kotulskite, merenskyite, michenerite), arsenides (sperrylite, guanglinite, majakite, etc.) and sulforasenides (hollingworthite, irarsite, platarsite) with dominating Pd minerals. The metal grade in the ore is 1–7 ppm total PGE at Pd/Pt = 3–5; 0.1–0.4 wt% Ni and 0.1–0.5 wt% Cu (Grokhovskaya et al., 2000).

### 1.7.2. Horizon 330 of Sopcha

The low-sulfide PGE mineralization of Horizon 330 is traced over its entire extent and occurs as separate interlayers. These are 10 cm to 1.5 m thick and closely related to sulfide disseminations. Fine sulfide disseminations (2–3 vol%) occur in the zone of intercalating harzburgites and orthopyroxenites. Their amount is up to 10 vol% in the orthopyroxenite zone. The disseminations are syngenetic and have no reaction relationships with primary silicates. At the same time, there is a distinct resorption of sulfides with late minerals (serpentine, chlorite, carbonate, and pyrite) (Neradovsky et al., 2002). Sulfide mineralization in harzburgites consists of pyrite, millerite, chalcopyrite, and pentlandite. In olivine pyroxenites and orthopyroxenites, it is represented by pyrrhotite, pentlandite, and chalcopyrite. Merenskyite, Pd-Pb, and Pd-Rh-Cu compounds are identified among PGM (Neradovsky et al., 2002; Mitrofanov & Smol'kin, 2004). In addition, Pd occurs as an admixture in pyrrhotite and chalcocite and Ir in pentlandite. The metal grades in the ore are as follows: 0.10–0.77 wt% Ni, 0.02–0.35 wt% Cu, up to 0.25 ppm Pt, and 1.6 ppm Pd at Pd/Pt = 4. The high Rh content (up to 0.1 ppm) is noted (Mitrofanov & Smol'kin, 2004).

### 1.7.3. Critical Horizon of Nyud

There are two horizons disseminated mineralization. The upper horizon is 5–30 m (up to 65 m) thick. It occupies an area of 700 × 300 m in hanging wall of olivine norites under the critical horizon represented by disseminated and less frequent stringer-disseminated mineralization and pockets of Cu and Ni sulfides. Pyrrhotite, pentlandite, and chalcopyrite dominate in the ore. Magnetite and ilmenite also occur. A segregation of the massive sulfide ore is mined out. It had a shape of a flattened cake, 6.75 m long, 3.5 m wide and 2 m thick. This ore body was composed of pyrrhotite (60–80 vol%), pentlandite (5–20 vol%), chalcopyrite (3–10%), and a great amount of fused silicate xenoliths. The highest Ni and Cu contents were 3.24 and 0.56 wt%, respectively.

The lower horizon occurs in the footwall of olivine norites at the contact with poikilitic norites. It is smaller and its thickness reaches 18.7 m. Fine- and stringer-disseminated ores with small pockets contain 0.2–0.3 wt% of Ni.

The Nyud-II deposit occurred 0.6 km to the SW of the Terrace deposit, hosted in melanocratic norites of the critical horizon. It was mined out in the early 1970s (Fig. 1.4). The sulfide Ni-Cu mineralization has a complex internal structure and comprises veinlet-schlieren, veinlet-disseminated and disseminated types. The veinlet-schlieren mineralization is economically best-valued. The schlieren are sulfide segregations, isometric in shape, and varying in size from a few decimeters to 5–7 m across. They occur at contacts of melanocratic and olivine norites with fine-grained norites and gabbronorites. The schlieren boundaries are both sharp and gradual due to surrounding microveinlets and disseminations. They frequently contain fused fragments of host norite and gabbronorite. The veinlet-disseminated type of mineralization is minor and mainly occurs at margins of schlieren. The disseminated mineralization is widespread as irregularly shaped ore bodies. They are tens of meters across and occur in various rocks (Bartenev & Dokuchaeva, 1975).

Sulfides are represented by pyrrhotite (40–50 vol%), chalcopyrite (20–30 vol%), pentlandite (10–15 vol%), and pyrite (5–10 vol%). There is magnetite as well (10–30 vol%). Mean PGE concentrations are 0.25 ppm Pt and 0.70 ppm Al; Pd/Pt = 2.8.

### 1.7.4. South Sopcha Deposit

The PGE mineralization is localized in various rocks from the lower marginal norite-pyroxenite zone of the South Sopcha deposit with fine (1–3 vol%) sulfide disseminations (Fig. 1.4). Structures of different ore zones within the deposit are markedly distinct. In the NW part, the ore zone consists of twenty 1–20 m-thick lenticular-stratal ore bodies. They occur throughout the lower zone section and become as thick as 50–60 m in total. In the SE part, the ore bodies are confined to the upper and middle parts of the lower zone and their number is reduced to 10. Their total thickness increases to 55–85 m, while the thickness of separate ore bodies varies from 1 to 65 m in bulges.

Three ore mineral assemblages are distinguished in the mineralized bodies: those with predominance of (1) pyrrhotite, (2) chalcopyrite and Ni-sulfides (violarite, polydymite, millerite, and pentlandite), and (3) sulfide disseminations spatially associated with titanomagnetite. The proportions of the sulfide amount vary widely. Pyrrhotite and pentlandite are frequently replaced with low-temperature marcasite, melnikovite, violarite, and pyrite, whereas chalcopyrite is replaced with chalcocite and covellite. Chalcopyrite and bornite lamellae are typical. Sulfides occur as disseminations and segregations of millerite-bornite-chalcopyrite and pentlandite-chalcopyrite-pyrrhotite assemblages. Their high contents (up to 5–10 vol%) are noted in pegmatoid norites and pyroxenites only. Here, the ore has high PGE contents (up to 0.5–0.9 ppm Pt + Pd). Minerals of the cobaltite-gersdorffite series with PGE admixtures frequently occur at the contact between the lower and upper zones of this massif (Grokhovskaya et al., 2012).

The PGE mineralization is represented by more than 20 mineral species. Palladium bismuthotellurides and arsenides are predominant. Merenskyite is the most abundant. Sperrylite occurs frequently. Sulfides of the braggite-cooperite-vysotskite series and other minerals are less abundant. The PGE grade of ores does not exceed 1–2 ppm with Pd/Pt = 3–4 (Grokhovskaya et al., 2012).

### 1.7.5. Lake Moroshkovoye Ore Occurrence

The ore body of this occurrence relates to the NW-trending thick tectonic zone in the western part of the massif at the contact of metagabbronorite with Archaean country diorites. The ore body is about 250 m long and up to 6 m thick. It is conformable to the foliation of tectonites, strikes in the NW direction, and dips to the NE at angles of 30°–70°. It is a combination of a veinlet, lenticular, and disseminated mineralization. Thin veinlets and lenses of massive sulfides consist of pyrrhotite-pyrite-chalcopyrite-pentlandite intergrowths. They are oriented conformably to foliation and occasionally contain host schist fragments. The disseminated mineralization is similar in composition and mostly clustered near lenses and veinlets of massive sulfides with sharp boundaries. It is also conformable to schistosity and emphasizes banded structure of the ore. Mean grades of the ore are 2.0 wt% Ni and 0.6 wt% Cu. The total PGE content reaches 1.85 ppm.

## 1.8. PETROGRAPHY OF SAMPLES

Eight samples have been taken for isotope analyses from the Nyud, Sopcha, Vurechuayvench, South Sopcha, and Lake Moroshkovoye massifs (Fig. 1.4). Two samples have been taken from of the Nyud-II critical horizon (Fig. 1.3). Sample B-65, weighing 68 kg, is composed of fine- to medium-grained olivine orthopyroxenites consisting of orthopyroxene (85–90 vol%), olivine (5 vol%), and plagioclase (1–2 vol%). Secondary minerals are represented by colorless amphibole (5 vol%), which replaces orthopyroxene; phlogopite and sulfides occur as sporadic grains. Sample B-66, weighing 62 kg, has been taken from mineralized medium- to fine-grained meso- to leucocratic taxitic norites (10–40 vol% orthopyroxene, 60–80 vol%

plagioclase, 1–2 vol% quartz). Secondary minerals are represented by colorless and pale green amphibole (2–3 vol%). It develops after orthopyroxene in combination with sulfides (1–3 vol%) and rare grains of accessory apatite.

Sample B-70, weighing 64 kg, has been taken from medium- to fine-grained harzburgites of Horizon 330 in the Sopcha massif (Fig. 1.4). It consists of olivine (65–70 wt%), orthopyroxene (20 vol%), secondary serpentine (5 vol%) replacing olivine, and colorless amphibole (5 vol%) after orthopyroxene and less frequent olivine, magnetite (up to 1 vol%), and sulfides (2–3 vol%).

Two geochronological samples have been taken from the Vurechuayvench massif. Sample B-58, weighing 67 kg, has been taken from fine-grained metaplagioclasite of the PGE-bearing reef (Fig. 1.1). The rock consists of intensely saussuritized (up to 60–70% clinozoisite and chlorite) and pelitized plagioclase (25–30 vol%) and quartz in interstices between plagioclase grains (up to 5 vol%). Amphibole, apatite, scapolite, and muscovite grains are rare. Ore minerals are represented by sulfides (up to 2 vol%). Sample B-59, weighing 62 kg, has been taken from medium-grained leucocratic metagabbronorites underlying PGE-bearing reef (Fig. 1.4). The sample contains (vol%): plagioclase (55–60), colorless amphibole (30), quartz (1–2), chlorite (10) after amphibole, and plagioclase and clinozoisite (2–3) after plagioclase.

Two samples have been taken from the South Sopcha massif. Sample B-63, weighing 44 kg, has been taken from fine-grained leucocratic metanorites of the lower PGE-bearing zone of the massif (Fig. 1.4). The sample contains (vol%): plagioclase (60–65), pale green amphibole (25–30), quartz (1–2), biotite (2–3), and chlorite (2–3) after amphibole and sulfides (2–3). Sample B-4, weighing 60 kg, has been taken from medium-grained mesocratic epidotized quartz-bearing metagabbro (Fig. 1.4). The sample contains (vol%): blue-green amphibole (50–60%), plagioclase (20%), epidote (15%), and quartz (5–10%). Ore minerals are represented by magnetite (2–3) and sporadic sulfide grains.

Sample B-61, weighing 65 kg, has been taken from medium-grained meso- to leucocratic metanorites of the Lake Moroshkovoye massif (Fig. 1.4). The sample contains (vol%): plagioclase (55–60%), orthopyroxene completely replaced with talc (30–40%), pale green amphibole (5%), and quartz (1–2%). Plagioclase is replaced with clinozoisite (2–3%) and amphibole with chlorite (1–2%). Ore minerals are represented by sporadic sulfide grains.

## 1.9. MONCHEGORSK ORE AREA: ISOTOPE U-PB DATA (ON SINGLE ZIRCON-BADDELEYITE)

The results are provided in Tables 1.1 and 1.2 and Fig. 1.5. Ten mg of zircon grains reflecting three morphotypes have been separated from olivine-bearing orthopyroxenite of the critical horizon in the Nyud-II deposit (sample B-65) (Table 1.2). The first variety is represented by crystal fragments with corroded surface 175 × 175 μm in size. The transparent grains are colored brown. No intraphase heterogeneity has been revealed in BSE images. The procedure of two-stage dissolution with separation of two portions has been applied to these zircons. The second zircon variety is characterized by isometric crystal fragments with a corroded surface 245 × 245 μm in size. The transparent grains are light lilac in color with slightly expressed zoning in BSE images. The near-concordant U-Pb age of these zircons is 2506 ± 3 Ma (Table 1.1). It is interpreted as the time of the orthopyroxenite crystallization in the critical horizon. The lower intersection of discordia with concordia is at the origin. Since the U-Pb system in zircon is not disturbed, this intersection can be considered to mark contemporary loss of Pb. The third zircon variety is crystal fragments with a corroded surface 175 × 175 μm in size. Transparent grains are light yellow in color, with poorly expressed zoning in BSE images. Their concordant age, corresponding to 2670 ± 4 Ma (Table 1.1), characterizes the xenocrystic origin

**Table 1.1** U-Pb Zircon (Zr) and Baddeleyite (Bd) Ages of Rocks from Monchegorsk Pluton.

| Massif | Rock | Age, Ma | Mineral | Source |
|---|---|---|---|---|
| NKT | Quartz norite | 2507 ± 9 | Zr | Mitrofanov & Smol'kin (2004); Bayanova (2004) |
| Nyud | Gabbro pegmatite | 2504.4 ± 1.5 | Zr | Amelin et al. (1995) |
| | Gabbro pegmatite | 2500 ± 5 | Zr, bad | Mitrofanov & Smol'kin (2004) |
| | Norite | 2493 ± 7 | Zr | Balashov et al. (1993) |
| Nyud-II | Orthopiroxenite | 2506 ± 3 | Zr | Chashchin et al. (2016) |
| | Ore norite | 2503 ± 8 | Zr | |
| Vurechuaivench | Metagabbronorite | 2497 ± 21 | Zr, bad | Mitrofanov & Smol'kin (2004) |
| | Metagabbronorite | 2498.2 ± 6.7 | Bad | Rundkvist et al. (2014) |
| | Metagabbronorite | 2504.2 ± 8.4 | Zr | |
| | Metaplagioclasite | 2507.9 ± 6.6 | Zr | |
| | Metagabbronorite | 2504.3 ± 2.2 | Zr | Chashchin et al. (2016) |
| | Ore plagioclasite | 2494 ± 4 | Zr | Chashchin et al. (2016) |

**Table 1.2** Isotopic U-Pb Data on Single Zircon Grains from Rocks of Monchegorsk Pluton and Massifs in its Southern Framing.

| No. | Weight, mg | Concentration, ppm | | Isotope ratios* | | | | Isotope ratios and age, Ma** | | | Dis., % |
|---|---|---|---|---|---|---|---|---|---|---|---|
| | | Pb | U | $^{206}Pb/^{204}Pb$ | $^{206}Pb/^{238}U \pm 2\sigma$ | $^{207}Pb/^{235}U \pm 2\sigma$ | $^{207}Pb/^{206}Pb \pm 2\sigma$ | $^{206}Pb/^{238}U \pm 2\sigma$ | $^{207}Pb/^{235}U \pm 2\sigma$ | $^{207}Pb/^{206}Pb \pm 2\sigma$ | |
| Metagabbronorite from Vurechuaivench massif (sample B-59) | | | | | | | | | | | |
| 1 | 0.0200 | 175.01 | 240.26 | 426.9 | 0.461 ± 0.003 | 10.465 ± 0.060 | 0.1649 ± 0.0002 | 2443 ± 14 | 2477 ± 14 | 2504 ± 3 | 2.4 |
| 2 | 0.0875 | 62.09 | 105.09 | 538.6 | 0.386 ± 0.001 | 8.773 ± 0.030 | 0.1527 ± 0.0003 | 2106 ± 6 | 2315 ± 8 | 2504 ± 4 | 15.9 |
| 3 | 0.0720 | 160.42 | 184.05 | 339.7 | 0.340 ± 0.002 | 7.738 ± 0.083 | 0.1418 ± 0.0013 | 1888 ± 12 | 2201 ± 24 | 2507 ± 20 | 24.7 |
| 4 | 0.0880 | 961.27 | 754.65 | 136.1 | 0.299 ± 0.002 | 4.258 ± 0.080 | 0.1009 ± 0.0017 | 1685 ± 11 | 1635 ± 31 | 1612 ± 27 | −4.5 |
| Mineralized metanorite from South Sopcha massif (sample B-63) | | | | | | | | | | | |
| 1 | 0.0043 | 29.36 | 17.71 | 541.2 | 0.477 ± 0.063 | 10.848 ± 1.508 | 0.1695 ± 0.0062 | 2504 ± 331 | 2505 ± 348 | 2508 ± 92 | 0.2 |
| 2 | 0.0114 | 133.33 | 308.70 | 578.4 | 0.392 ± 0.002 | 7.149 ± 0.046 | 0.1323 ± 0.0002 | 2132 ± 13 | 2130 ± 14 | 2129 ± 4 | −0.1 |
| Metagabbro from South Sopcha massif (sample B-64) | | | | | | | | | | | |
| 1 | 0.0984 | 40.78 | 40.28 | 60.9 | 0.420 ± 0.002 | 9.196 ± 0.184 | 0.1545 ± 0.0026 | 2066 ± 21 | 2237 ± 24 | 2358 ± 41 | 15.9 |
| 2 | 0.0700 | 129.13 | 201.22 | 207.5 | 0.378 ± 0.004 | 8.149 ± 0.088 | 0.1526 ± 0.0004 | 1984 ± 11 | 2174 ± 4 | 2396 ± 7 | 13.8 |
| 3 | 0.2000 | 67.72 | 134.61 | 489.2 | 0.336 ± 0.005 | 7.078 ± 0.105 | 0.1511 ± 0.0006 | 1869 ± 26 | 2121 ± 31 | 2376 ± 10 | 21.3 |
| Metanorite from massif of Lake Moroshkovoe (sample B-61) | | | | | | | | | | | |
| 1 | 0.0800 | 67.60 | 70.85 | 1352.7 | 0.436 ± 0.003 | 9.663 ± 0.063 | 0.1646 ± 0.0003 | 2287 ± 14 | 2403 ± 16 | 2503 ± 4 | 8.6 |
| 2 | 0.0212 | 60.48 | 71.14 | 325.5 | 0.380 ± 0.003 | 8.408 ± 0.069 | 0.1626 ± 0.0005 | 2074 ± 16 | 2287 ± 19 | 2483 ± 7 | 16.5 |
| 3 | 0.0200 | 2.38 | 12.06 | 144.8 | 0.060 ± 0.003 | 7.361 ± 0.066 | 0.1612 ± 0.0038 | 377 ± 16 | 872 ± 43 | 2497 ± 57 | 84.9 |

*All ratios are corrected to blank contamination (0.08 ng Pb, 0.04 ng U) and to mass discrimination 0.12 ± 0.04%.
**Correction to common lead has been determined by age according to model of Stacey and Kramers (1975).